ACCEPTED VERSION

Ng, C.T.
[Bayesian model updating approach for experimental identification of damage in beams using guided waves](), Structural Health Monitoring, 2014; 13(4):359-373.

http://hdl.handle.net/2440/85788

Bayesian model updating approach for experimental identification of damage in beams using guided waves

Ching-Tai Ng

School of Civil, Environmental & Mining Engineering, The University of Adelaide, SA, Australia

Author to whom correspondence should be addressed:

Ching-Tai Ng

School of Civil, Environmental & Mining Engineering, The University of Adelaide, SA, 5005, Australia

Email: alex.ng@adelaide.edu.au

Abstract

A Bayesian approach is proposed to quantitatively identify damages in beam-like structures using experimentally measured guided wave signals. The proposed methodology treats the damage location, length and depth as unknown parameters. Damage identification is achieved by solving an optimization problem, in which a hybrid particle swarm optimization (PSO) algorithm is applied to maximize the probability density function (PDF) of a damage scenario conditional on the measured guided wave signals. Signal envelopes extracted by the Hilbert transform are proposed to minimize the complexity of the optimization problem in order to enhance the robustness and computational efficiency of the damage identification. One of the advantages of the proposed methodology is that instead of only pinpointing the multivariate damage characteristics, the uncertainty associated with the damage identification results is also quantified. This outcome provides essential information for making decisions about the remedial work necessary to repair structural damage. The experimental data consists of guided wave signals measured at a single location of the beams. A number of experimental case studies considering damages of different scenarios are used to demonstrate the success of the proposed Bayesian approach in identifying the damages. The results show that the proposed approach is able to accurately identify damages, even when the extent of the damage is small.

Introduction

Infrastructure plays an important role in our daily life. It enhances access to public services and both physical and service sector resources (e.g., bridges, buildings, aerospace, pipeline, wind energy generation as well as land and water transport infrastructure). The aging and deterioration of engineered infrastructure across the developed world have therefore become a universal challenge for governments and industries. Thus, monitoring structural integrity to enhance the sustainability and reliability of both new and old structures, and the reduction of their life cycle costs have become increasingly important.

Accumulation of damage over the lifespan of a structure without adequate and timely inspection can lead to catastrophic failure. Various damage detection techniques have been developed over many years. These are typified by conventional ultrasonic, acoustic emission, eddy-current, vibration-based and guided wave techniques[1-7]. Vibration-based and guided wave techniques in particular have attracted much attention. Vibration-based techniques detect damages using the dynamic characteristics of structures have been extensively studied in the last two decades[8-12] but detection of damage mainly depends on successfully recognising changes in the vibration characteristics of the structures being tested. Guided wave techniques, on the other hand, use mechanical stress waves propagated at ultrasonic frequencies along natural boundaries in the structural material to detect damage using a pulse-echo or pitch-catch configuration of transducers. The object being tested is therefore, in essence, a waveguide. Guided waves are regarded as sensitive and efficient at detecting both small and different types of damages in structures, and have been reported as capable of monitoring large areas of a structure due to their ability to propagate over long distances[13-18].

Recent years have shown growing interest in using vibro-acoustic modulation technique for damage detection. This technique employs the nonlinear interaction of high-frequency ultrasonic wave and low-frequency vibration excitation. Donskoy et al.[19] proposed two approaches using the nonlinear effect of modulation of ultrasonic wave by forced harmonic

vibration and impact excitation of natural modes of vibration of structure, respectively. They demonstrated that the resulting modulated signal contains new frequency components, which are can be used to detect the defect in the structures. Yoder and Adams[20] proposed a swept probing signal to increase the applicability and robustness of the vibro-acoustic modulation technique in damage detection with experimental verification. Klepka et al.[21] carried out an experimental investigation of the low-frequency vibration excitation on modulation intensity and associated nonlinear wave interaction mechanisms, which further enhanced the understanding of using the vibro-acoustic modulation technique in damage detection.

Guided waves can propagate in different types of structures that are generally categorized into one- and two-dimensional waveguides. Examples of one-dimensional waveguides are beams and pipes. Some research has investigated the guided wave propagation and scattering phenomenon at defects in beams[22] and pipes[23-25], and demonstrated the guided waves are sensitive to the defects. Two-dimensional waveguides are represented by structural components such as plates and shells. Most research into the use of guided waves for locating and characterizing damage relates to two-dimensional waveguides. Relatively less work has focused on beams, especially for damage characterization, i.e. identifying damage location and severity.

Beam-like structures, one of the most common types of structural components, particularly in civil and mechanical engineering, are essentially one-dimensional waveguides for guided wave testing. In the literature some research has investigated the use of guided waves for detecting and locating damages in this type of structures. These studies have especially focused on crack detection. Quek et al.[26], for example, employed the impulse wave generated by impact excitation to locate cracks in aluminium beams. Experimentally measured wave signals were processed using the Hilbert-Huang transform to determine crack locations. Li et al.[27] proposed a method of detecting damage based on a continuous wavelet transform of flexural wave signals. The results of their experiments showed that cracks can

be located based on the arrival time of the reflected wave, but that the size of the crack can only be qualitatively estimated. Grabowska *et al.*[28] employed the wavelet transform to decompose a guided wave for damage detection. The study demonstrated that the wavelet decomposed guided wave signal can be used to distinguish different kinds of damages. Sun *et al.*[29] reported on research into the use of a guided wave to locate a crack in thick steel beams, which demonstrated the potential for judging crack size based on the time delay of the transmitted wave. Zhu *et al.*[30] proposed a method of detecting the presence of cracks in trusses using guided waves. The results of their experiments indicated that the cracks can be detected using the extracted defect-sensitive features in the outlier analysis. The method was verified using a truss structure in experiments.

Overall, current research indicates that the arrival time and amplitude of reflected waves can be used to locate cracks with roughly estimation of their sizes. When dealing with less egregious, more subtle damage, however, such approaches face many challenges. Laminar types of damages, such as corrosion thinning, for example, are difficult to characterize because the behaviour of the waves reflected from laminar damages is much more complicated than the behaviour of waves reflected from cracks. More than one reflected wave pulse can be observed from the laminar damage as wave reflections happen when incident pulses both enter and leave the laminar damage.

While the majority of research development has focused on detecting the damage, limited research[31,32] has confronted damage identification. Model-based approaches have, for example, been suggested to quantitatively identify damage. Krawczuk[33] proposed an iterative search technique to identify cracks in beam-like structures using flexural waves. A genetic algorithm combined with a gradient method formed the search technique for damage identification. Numerical case studies were used to verify the proposed method and the results indicated that it performed better than methods based on changes in modal parameters. Ng *et al.*[34] numerically investigated the sensitivity of longitudinal waves in terms of their

ability to quantitatively identify damages of different sizes and with different measurement noise levels. An optimization approach was proposed to identify the damage in the study. Pau and Vestroni[35] employed transient responses excited by an impulsive force to identify step damage in a one-dimensional waveguide. The damage was identified by comparing the analytical and experimental reflected and transmitted wave signals. On the whole, in the literature the majority of studies have focused more on damage detection than on identification. Although there have been limited developments for quantitative identification of damages using guided waves, limited work has experimental verifications to demonstrate the feasibility of practical applications.

The current study presents a Bayesian statistical framework[36] for experimental identification of the laminar damage in beam-like structures. The Bayesian statistical framework was originally developed for damage detection based on model updating approach with low frequency vibration data. This study extends the framework to quantitative damage identification by using guided wave signals as the measured data. Unlike most of the existing guided wave based damage detection methods, the proposed Bayesian approach identifies the damages by maximizing the probability density function (PDF) conditional on measured longitudinal guided wave signals.

In the proposed approach, damage parameters of the numerical beam model are treated as unknowns and updated to identify the damage. In this study the numerical beam model is developed using a frequency domain spectral finite element method based on the Mindlin-Herrmann theory, which enhances the robustness and computational efficiency of the damage identification. The model updating is achieved by solving the optimization problem, in which the discrepancy of the measured and predicted guided wave signals is minimized by changing the damage parameters of the numerical beam model.

Given the difference of the nature between the guided wave signals and the low frequency vibration data, improvements are proposed to overcome the challenges of

extending the Bayesian statistical framework to practical damage identification using guided waves. The current study enhances the Bayesian statistical framework by using the signal envelopes as the data in the damage identification, which substantially reduces the complexity of the optimization problem. A hybrid particle swarm optimization (PSO) algorithm is adapted to further improve the robustness and efficiency of the damage identification process. These improve the applicability of the proposed Bayesian approach in practical situation. One of the important contributions of the paper is to provide an in-depth exploration of the Bayesian statistical framework in quantitative identification of damage using experimentally measured guided waves. Instead of pinpointing the damage location and extent as in most of the existing methods, the proposed Bayesian approach also quantifies the uncertainties associated with the damage identification results, which is particularly important for making decisions about necessary remedial work. The proposed Bayesian approach is experimentally verified using a guided wave signal measured at a single location in the beam-like structure.

The remainder of this paper is organized as follows. The frequency spectral finite element method based on the Mindlin-Herrmann theory is presented first. The proposed damage identification method is then provided in section "Bayesian approach for damage characterization", along with a description of a posterior PDF of uncertain damage parameters calculation. The signal envelope extraction using the Hilbert transform and the Hybrid PSO algorithm are then presented. A study of the measurement position effect on guided wave signals is presented in section "Measurement position effect on guided wave signals". The experimental setup is outlined in section "Experimental verification". In the same section the damage identification results of a number of experimental case studies are discussed in detail. Finally, the conclusions are drawn in section "Conclusions".

Modelling of longitudinal wave in beams with damages

Mindlin-Herrmann theory

As opposed to the single mode theory such as elementary and Love theories, the Mindlin-Hermann theory[37] describes the longitudinal wave using two coupled partial differential equations. It has been shown that the single mode theory cannot be sufficient to capture the wave propagation phenomenon for thick beams and/or high frequency wave[22,38], which is the situation of the current study. Hence the Mindlin-Herrmann theory was employed to model the longitudinal guided wave in the beam. The Mindlin-Herrmann theory modifies the Love theory to take into account the shearing deformation due to the transverse displacement but retaining the Poisson's ratio relation between the axial and transverse strains, and assumes that the transverse deformation is independent of the axial contraction. It should be noted that the beam model in this study does not consider effect of mode conversion from longitudinal wave to flexural wave at the step damage, hence, only longitudinal wave is modelled in the study. The section "Preliminary study of measurement position effect on guided wave signals" will discuss the guided wave signals measured at different positions at the beam cross-section, which shows that the flexural wave induced by mode conversion can be excluded in the measured signals by choosing an appropriate measurement position. The study shows that the understanding of the wave propagation phenomenon can be used to simplify the beam model in the damage identification.

In the Mindlin-Hermann theory, a finite element has two nodes with two degrees-of-freedom per node, longitudinal $u_j(x,y,t)$ and lateral $v_j(x,y,t)$ displacements, and they are defined as

$$u_j\left(x,y,t\right) \approx \bar{u}_j\left(x,t\right), \qquad v_j\left(x,y,t\right) \approx y\bar{\phi}_j\left(x,t\right) \tag{1}$$

where $\bar{u}_j$ and $\bar{\phi}_j$ are the horizontal displacement and rotational angle on the neutral axis of the beam. Based on the Mindlin-Herrmann, the governing equations for the wave propagation problem[37] are

$$\left(2\mu_j + \lambda_j\right)A_j\frac{\partial^2 \bar{u}_j}{\partial x^2} + \lambda_j A_j \frac{\partial \bar{\phi}_j}{\partial x} = \rho_j A_j \frac{\partial^2 \bar{u}_j}{\partial t^2}$$
$$\mu_j I_j S_1 \frac{\partial^2 \bar{\phi}_j}{\partial x^2} - \left(2\mu_j + \lambda_j\right)A_j\bar{\phi}_j - \lambda_j A_j \frac{\partial \bar{u}_j}{\partial x} = \rho_j I_j S_{2,j} \frac{\partial^2 \bar{\phi}_j}{\partial t^2} \tag{2}$$

where μ_j and λ_j are Lame constants and equal to $E_j/(2(1+v_j))$ and $v_j E_j/((1+v_j)(1-2v_j))$, respectively. v_j is the Poisson's ratio. E_j, $A_j = b_j h_j$, $I_j = b_j h_j^3/12$ and ρ_j are the Young's modulus, cross-section area, second moment of area and density. b_j and h_j are the width and thickness of the beam. S_1 and $S_{2,j}$ are correction factors introduced to account both for the non-symmetry of the cross-section and the fact that the actual stresses are not distributed as assumed[37]. $S_1 = 12/\pi^2$ and $S_{2,j} = S_1((1+v_j)/(0.87+1.12v_j))^2$. Using the Mindlin-Hermann theory the shearing deformation due to the transverse displacement is also taken into account in the prediction of the longitudinal wave propagation, which provides a more accurate prediction compared to elementary and Love theories.

Frequency domain spectral finite element method

In this study the frequency domain spectral finite element method[37] is developed based on the Mindlin-Herrmann theory discussed in the last section. The method is essentially a finite element method formulated in the frequency domain. One of the advantages of using frequency domain spectral finite element method is that it not only gives the flexibility of conventional finite element modelling but also accurately simulates the wave propagation with much higher computational efficiency. Hence it is particularly suitable for damage identification through solving an inverse problem.

As shown in Figure 1, a frequency domain spectral finite element based on the Mindlin-Herrmann theory with length L_j was used to model the longitudinal guided wave in this study. The spectral representations for the response variables were

$$u_j(x,t) = \sum_{n=1}^{N} \hat{u}_{n,j}(x,\omega_n) e^{i\omega_n t}, \qquad \phi_j(x,t) = \sum_{n=1}^{N} \hat{\phi}_{n,j}(x,\omega_n) e^{i\omega_n t} \qquad (3)$$

where $\hat{u}_{n,j}$ and $\hat{\phi}_{n,j}$ are the Fourier coefficients associated with the response variables u_j and ϕ_j at n-th angular frequency ω_n. i is the imaginary unit. The summation is carried out up to the Nyquist frequency ω_N. By substituting equation (3) into equation (2), the partial differential equations are reduced to two sets of ordinary differential equations with the time variation removed[39] as

$$-(2\mu_j + \lambda_j) A_j \frac{\partial^2 \hat{u}_{n,j}}{\partial x^2} - \rho_j A_j \omega_n^2 \hat{u}_{n,j} - \lambda_j A_j \frac{\partial \hat{\phi}_{n,j}}{\partial x} = 0$$

$$\lambda_j A_j \frac{\partial \hat{u}_{n,j}}{\partial x} - \mu_j I_j S_1 \frac{\partial^2 \hat{\phi}_{n,j}}{\partial x^2} + (2\mu_j + \lambda_j) A_j \hat{\phi}_{n,j} - \rho I_j S_{2,j} \omega_n^2 \hat{\phi}_{n,j} = 0 \qquad n = 1, ..., N \qquad (4)$$

The general response variables in the frequency domain are written as

$$\hat{u}_{n,j}(x,\omega_n) = U_j e^{-i(k_j x - \omega_n t)}, \qquad \hat{\phi}_{n,j}(x,\omega_n) = \Phi_j e^{-i(k_j x - \omega_n t)} \qquad (5)$$

where k_j denotes a wavenumber corresponding to ω_n. U_j and Φ_j are amplitude spectrums at n-th angular frequency ω_n. Substituting equation (5) into equation (4), the characteristic equation for the solution of the wavenumber is obtained as

$$\begin{bmatrix} -k_j^2 (2\mu_j + \lambda_j) A_j + \rho_j A_j \omega_n^2 & -ik_j \lambda_j A_j \\ ik_j \lambda_j A_j & -\mu_j I_j S_1 - (2\mu_j + \lambda_j) A_j + \rho_j I_j S_{2,j} \omega_n^2 \end{bmatrix} \begin{Bmatrix} U_j \\ \Phi_j \end{Bmatrix} = 0 \qquad (6)$$

where the unknowns are k_j, U_j and Φ_j. Equation (6) can be rearranged to a second order standard polynomial eigenvalue problem as

$$\{k_j^2 \mathbf{B}_{2,j} + k_j \mathbf{B}_{1,j} + \mathbf{B}_{0,j}\} \begin{Bmatrix} R_{1,j} \\ R_{2,j} \end{Bmatrix} = 0 \qquad (7)$$

where
$$\mathbf{B}_{2,j} = \begin{bmatrix} -\left(2\mu_j + \lambda_j\right)A_j & 0 \\ 0 & -\mu_j I_j S_1 \end{bmatrix} \quad , \quad \mathbf{B}_{1,j} = \begin{bmatrix} 0 & -ik_j\lambda_j A_j \\ ik_j\lambda_j A_j & 0 \end{bmatrix} \quad ,$$

$$\mathbf{B}_{0,j} = \begin{bmatrix} \rho_j A_j \omega_n^2 & 0 \\ 0 & -\left(2\mu_j + \lambda_j\right)A_j + \rho_j I_j S_{2,j}\omega_n^2 \end{bmatrix}$$

There are four eigenvalues (k_j) and eigenvectors $\left\{U_j \quad \Phi_j\right\}^T$, which can be solved by the QZ algorithm[40] and the eigenvectors are arranged in a matrix $\mathbf{R}_j = \left\{R_{1,j} \quad R_{2,j}\right\}^T$. The general solution at frequency ω_n can then be written as

$$\begin{Bmatrix} \hat{u}_{n,j}(x) \\ \hat{\phi}_{n,j}(x) \end{Bmatrix} = \sum_{m=1}^{2} C_{m,j}\begin{Bmatrix} R_{1m,j} \\ R_{2m,j} \end{Bmatrix} e^{-ik_{m,j}x} + \sum_{m=3}^{4} C_{m,j}\begin{Bmatrix} R_{1m,j} \\ R_{2m,j} \end{Bmatrix} e^{ik_{m,j}(L_j - x)} \tag{8}$$

where $C_{m,j}$ for $m = 1,2,3,4$ are unknown coefficients to be determined from the boundary conditions at the left and right ends of the spectral element. As shown in Figure 1, the responses at the both ends of the spectral element are

$$\hat{u}_{n,j}(0) = \hat{u}_{\alpha,j}, \quad \hat{\phi}_{n,j}(0) = \hat{\phi}_{\alpha,j} \text{ and } \hat{u}_{n,j}(L_j) = \hat{u}_{\beta,j}, \quad \hat{\phi}_{n,j}(L_j) = \hat{\phi}_{\beta,j} \tag{9}$$

The relationship between the spectral longitudinal displacement and the lateral contraction with the unknown coefficient $C_{m,j}$ can be expressed as

$$\boldsymbol{\delta}_j = \mathbf{T}_{1,j}\mathbf{C}_j \tag{10}$$

where $\boldsymbol{\delta}_j = \left\{\hat{u}_{\alpha,j} \quad \hat{\phi}_{\alpha,j} \quad \hat{u}_{\beta,j} \quad \hat{\phi}_{\beta,j}\right\}^T$, $\mathbf{C}_j = \left\{C_{1,j} \quad C_{2,j} \quad C_{3,j} \quad C_{4,j}\right\}^T$ and

$$\mathbf{T}_{1,j} = \begin{bmatrix} R_{11,j} & R_{12,j} & R_{13,j}e^{ik_{3,j}L_j} & R_{14,j}e^{ik_{4,j}L_j} \\ R_{21,j} & R_{22,j} & R_{23,j}e^{ik_{3,j}L_j} & R_{24,j}e^{ik_{4,j}L_j} \\ R_{11,j}e^{-ik_{1,j}L_j} & R_{12,j}e^{-ik_{2,j}L_j} & R_{13,j} & R_{14,j} \\ R_{21,j}e^{-ik_{1,j}L_j} & R_{22,j}e^{-ik_{2,j}L_j} & R_{23,j} & R_{24,j} \end{bmatrix}$$

The nodal spectral axial force and shear force at the left ($x = 0$) and right ends ($x = L_j$) are

$$\hat{F}_{\alpha,j} = -\left[\left(2\mu_j + \lambda_j\right)A_j \frac{\partial \hat{u}_j\left(0,\omega_n\right)}{\partial x} + \lambda_j A_j \hat{\phi}_j\left(0,\omega_n\right)\right], \quad \hat{Q}_{\alpha,j} = -\mu_j I_j S_1 \frac{\partial \hat{\phi}_j\left(0,\omega_n\right)}{\partial x} \quad (11)$$

$$\hat{F}_{\beta,j} = -\left[\left(2\mu_j + \lambda_j\right)A_j \frac{\partial \hat{u}_j\left(L_j,\omega_n\right)}{\partial x} + \lambda_j A_j \hat{\phi}_j\left(L_j,\omega_n\right)\right], \quad \hat{Q}_{\beta,j} = -\mu_j I_j S_1 \frac{\partial \hat{\phi}_j\left(L_j,\omega_n\right)}{\partial x} \quad (12)$$

Using these boundary conditions, the relationship between the nodal spectral forces and the unknown coefficients $C_{m,j}$ can be expressed as

$$\mathbf{F}_j = \mathbf{T}_{2,j}\mathbf{C}_j \quad (13)$$

where $\mathbf{F}_j = \left\{\hat{F}_{\alpha,j} \quad \hat{Q}_{\alpha,j} \quad \hat{F}_{\beta,j} \quad \hat{Q}_{\beta,j}\right\}^T$ and

$$\mathbf{T}_{2,j} = \begin{bmatrix} ik_{1,j}\Delta_{1,j}R_{11,j} - \Delta_{2,j}R_{21,j} & ik_{2,j}\Delta_{1,j}R_{12,j} - \Delta_{2,j}R_{22,j} & \left(ik_{3,j}\Delta_{1,j}R_{13,j} - \Delta_{2,j}R_{23,j}\right)e^{ik_{3,j}L_j} & \left(ik_{4,j}\Delta_{1,j}R_{14,j} - \Delta_{2,j}R_{24,j}\right)e^{ik_{4,j}L_j} \\ ik_{1,j}\Delta_{3,j}R_{21,j} & ik_{2,j}\Delta_{3,j}R_{22,j} & ik_{3,j}\Delta_{3,j}R_{23,j}e^{ik_{3,j}L_j} & ik_{4,j}\Delta_{3,j}R_{24,j}e^{ik_{4,j}L_j} \\ \left(-ik_{1,j}\Delta_{1,j}R_{11,j} + \Delta_{2,j}R_{21,j}\right)e^{-k_{1,j}L_j} & \left(-ik_{2,j}\Delta_{1,j}R_{12,j} + \Delta_{2,j}R_{22,j}\right)e^{-k_{2,j}L_j} & -ik_{3,j}\Delta_{1,j}R_{13,j} + \Delta_{2,j}R_{23,j} & -ik_{4,j}\Delta_{1,j}R_{14,j} + \Delta_{2,j}R_{24,j} \\ -ik_{1,j}\Delta_{3,j}R_{21,j}e^{-k_{1,j}L_j} & -ik_{2,j}\Delta_{3,j}R_{22,j}e^{-k_{2,j}L_j} & -ik_{3,j}\Delta_{3,j}R_{23,j} & -ik_{4,j}\Delta_{3,j}R_{24,j} \end{bmatrix} \quad (14)$$

where $\Delta_{1,j} = \left(2\mu_j + \lambda_j\right)A_j$, $\Delta_{2,j} = \lambda_j A_j$ and $\Delta_{3,j} = \mu_j I_j S_1$. The dynamic stiffness matrix $\mathbf{K}_{\omega_n,j}$ can be obtained by $\mathbf{T}_{2,j}\mathbf{T}_{1,j}^{-1}$.

Throw-off element for modelling semi-infinite and infinite beams

As opposed to the conventional finite element method, the frequency domain spectral finite element method allows modelling semi-infinite and infinite beams without using a large number of elements, which substantially enhances the computational efficiency of modelling wave propagation in large structures. Guided wave is generated by a transient excitation and then propagates from the excitation location with no secondary disturbances. For a long beam, the guided wave reflection from the boundaries can be neglected because of attenuation after a long travel distance or if the wave does not reach the desired location within the timeframe of the observation. To further reduce the computational time of solving the inverse problem for damage identification, this section presents a formulation of a throw-off element for simulating a non-reflecting boundary condition for wave propagation problems. Considering

a throw-off spectral element with a non-reflecting boundary at the right end, the unknown constants $C_{3,j}$ and $C_{4,j}$ in equation (8) can be ignored because they represent the wave propagating toward the left end of the beam. The matrices $\mathbf{T}_{1,j}$ and $\mathbf{T}_{2,j}$ can then be reduced to

$$\mathbf{T}_{1,j} = \begin{bmatrix} R_{11,j} & R_{12,j} \\ R_{21,j} & R_{22,j} \end{bmatrix} \tag{15}$$

$$\mathbf{T}_{2,j} = \begin{bmatrix} ik_{1,j}\Delta_{1,j}R_{11,j} - \Delta_{2,j}R_{21,j} & ik_{2,j}\Delta_{1,j}R_{12,j} - \Delta_{2,j}R_{22,j} \\ ik_{1,j}\Delta_{3,j}R_{21,j} & ik_{2,j}\Delta_{3,j}R_{22,j} \end{bmatrix} \tag{16}$$

The dynamic stiffness matrix for the throw-off element can be obtained by $\tilde{\mathbf{K}}_{\omega_n,j} = \mathbf{T}_{2,j}\mathbf{T}_{1,j}^{-1}$.

Damaged beam model

With the frequency domain spectral finite element and the throw-off element developed in the last two sections, a damaged semi-infinite beam is modelled using three spectral finite elements and a throw-off element. The damaged beam model is then used for damage identification following the Bayesian approach in the next section. The throw-off element is located at the right end of the beam, and therefore, no wave is reflected from the right beam end. In this study a step damage is modelled by reducing the cross-sectional area of a beam region with length d_L. The location of the damage L_d is defined as the distance from the left beam end to the left end of the step damage. The cross-section area reduction of the damage can be calculated based on the depth d_d of the step damage as $b(h - d_d)$. The step damage is parameterized by L_d, d_L and d_d, which control the damage location, length and depth. In reality, there exists some uncertainty in the beam material properties and the Mindlin-Herrmann theory in the spectral element method does not fully account for the three-dimensional (3D) effects on the longitudinal wave propagation in beams with a

rectangular cross-section. Hence, Young's modulus is also included as an uncertain parameter in the optimization problem. The proposed Bayesian approach was used to identify the damage in the beam.

Bayesian approach for damage characterization

Damage identification is an inverse problem. Damage is detected and identified from measured data. However, the number of sensors that can be installed on structures is limited and measurements always contain noise in real world situations. Damage identification results are therefore always associated with uncertainties that may lead to incorrect decisions about remediation. In attempts to overcome these issues, statistical approach has been employed to address the issue of limited number of sensors[41,42] and handle the uncertainties in damage detection. Beck and Katafygiotis[36] proposed a Bayesian statistical framework for damage detection using low frequency vibration characteristics of structures, e.g. natural frequencies and modeshapes. The framework was also applied to structural health monitoring applications[43] but it has not yet been fully explored for damage detection using guided waves. Recently the maximum likelihood approach was employed to determine the location of damage using guided waves[44,45].

In the current study the Bayesian statistical framework[36] was extended to provide a quantitative identification of damage using guided waves. The extended approach is experimentally verified to demonstrate its applicability in real situation. The proposed method not only identifies the damage in the beams, but also quantifies the uncertainties associated with the damage identification results. The uncertainty information of the damage identification results is particularly important for engineers and infrastructure managers who are trying to make judgements about remedial work, especially in situations where the damage is in inaccessible locations. In the following sections the Bayesian statistical

framework is first introduced. The details of calculating the posterior PDF of the unknown damage parameters are then discussed. Damage identification was achieved by maximizing the likelihood function in the Bayesian statistical framework using a hybrid PSO algorithm.

Bayesian statistical identification framework

The Bayesian statistical identification framework[36] embeds a class of deterministic structural models M within a class of probability models. This arrangement allows for guided wave response predictions $u(t;\boldsymbol{\theta})$ and modelling of prediction error $e(t,\boldsymbol{\theta})$. $\boldsymbol{\theta}$ are the uncertain structural parameters chosen from a set of possible parameter values from a region $\Gamma(\boldsymbol{\theta})$. The prediction error $e(t,\boldsymbol{\theta})$ is defined as the difference between the predicted and the measured guided wave responses, which may be the result of measurement noise and modelling error. A class of probability models $P(\sigma)$ is required that must be parameterized by a parameter σ which is selected to be the standard deviation of the underlying PDF of the prediction error $e(t,\boldsymbol{\theta})$. By selecting the classes of M and P, the class of structural and probability models M_P can be defined and parameterized by $\mathbf{a} = \{\boldsymbol{\theta}^T, \sigma\}^T \in S(\mathbf{a})$. In the damage identification process, a set of guided wave responses D can be obtained through measurements. Using the Bayes' theorem, the posterior PDF of $\mathbf{a}$ for a given set of measured guided wave data D and a given class of structural and probability models M_P can be calculated as

$$p(\mathbf{a}\,|\,D, M_P) = cp(D\,|\,\mathbf{a}, M_P)\,p(\mathbf{a}\,|\,M_P) \qquad (17)$$

where $p(\mathbf{a}\,|\,M_P) = \pi(\mathbf{a})$ is the prior PDF of $\mathbf{a}$ over the set $S(\mathbf{a})$ of possible parameter values. The prior PDF can be chosen as a smooth and slowly-varying PDF to roughly reflect the engineer's judgement of the relative plausibility of the different values of the parameters

a and achieve a mathematical convenience. c is a normalizing constant such that the expression on the left-hand side of equation (17) is equal to unity and can be defined as

$$c = \frac{1}{\int_{S(\mathbf{a})} p(D \mid \mathbf{a}, M_P) p(\mathbf{a} \mid M_P) d\mathbf{a}} \tag{18}$$

It is common that the signal-to-noise ratio of the measured guided wave signals is improved by averaging the signals over number acquisitions. Hence the measurement noise is generally very small and the prediction error $e(t, \boldsymbol{\theta})$ is mainly due to the modelling error. It is assume that the prediction error $e(t, \boldsymbol{\theta})$, which is the discrepancy between predicted signals simulated by the numerical model and experimentally measured signals, is normally distributed and can be approximated by Gaussian distribution. In this case the likelihood of observing the data given the parameters **a** from the class of models M_P, $p(D \mid \mathbf{a}, M_P)$, in equation (17) can be written as

$$p(D \mid \mathbf{a}, M_P) = \left(\sqrt{2\pi} \sigma \right)^{-N_t N_o} \exp\left[-\frac{1}{2\sigma^2} \sum_{t=1}^{N_t} \left\| \tilde{u}(t) - u(t; \boldsymbol{\theta}) \right\|^2 \right] \tag{19}$$

where $\tilde{u}(t)$ is the measured guided wave signal at the t-th time step; $u(t; \boldsymbol{\theta})$ is the predicted guided wave signal based on the model class M_P for a given set of uncertain parameters $\boldsymbol{\theta}$; N_o is the number of measurement points, equivalent to the number of laser measurement points/transducers in the experiments; N_t is the number of time steps in the measurements; $\|\cdot\|$ denotes the standard Euclidean norm of the second kind.

Posterior PDF of uncertain damage parameters

The posterior PDF of the uncertain damage parameter $p(\boldsymbol{\theta} \mid D, M_P)$ can be obtained from equation (17) by integrating σ as

$$p(\boldsymbol{\theta} \mid D, M_P) = \int_0^\infty c p(D \mid \boldsymbol{\theta}, \sigma, M_P) \pi(\boldsymbol{\theta}, \sigma) d\sigma \tag{20}$$

As the number of measured time steps N_t is sufficiently large, it can be assumed that the prior distribution $p(\mathbf{a} \mid M_P) = \pi(\mathbf{a})$ is a slowly varying function of σ; the value of $p(\boldsymbol{\theta} \mid D, M_P)$ becomes negligible everywhere, except for the region of the parameter space where the posterior PDF of the uncertain parameters $\boldsymbol{\theta}$ is close to its global maximum at the value

$$\hat{\sigma}^2\left(\hat{\boldsymbol{\theta}}\right) = J\left(\hat{\boldsymbol{\theta}}\right) = \frac{1}{N_t N_0} \sum_{t=1}^{N_t} \left\| \tilde{u}(t) - u\left(t; \hat{\boldsymbol{\theta}}\right) \right\|^2 \tag{21}$$

where $J(\boldsymbol{\theta})$ is a measure-of-fit function between the predicted and measured guided wave signals. The integral in equation (20) can be approximated[46] as

$$p\left(\boldsymbol{\theta} \mid D, M_P\right) = c_1 J\left(\boldsymbol{\theta}\right)^{(N_t N_o - 1)/2} \pi\left(\boldsymbol{\theta}, \hat{\sigma}\left(\boldsymbol{\theta}\right)\right) \tag{22}$$

where c_1 is another normalizing constant. In this situation, the region of important probabilities locally extends around the points that globally minimize $J(\boldsymbol{\theta})$. $\hat{\sigma}^2$ is the optimal variance in the prediction error model. In identifiable cases, there is either one optimal value for $\boldsymbol{\theta}$ or more than one optimal value, but the distance between the optimal values is finite within region $S(\boldsymbol{\theta})$. The posterior PDF of the uncertain parameter vector $\boldsymbol{\theta}$ can be approximated by a weighted sum of Gaussian distributions centred at R optimal points as

$$p\left(\boldsymbol{\theta} \mid D, M_P\right) \approx \sum_{r=1}^{R} \frac{\pi\left(\hat{\boldsymbol{\theta}}^{(r)}\right) \left| \mathbf{A}_N\left(\hat{\boldsymbol{\theta}}^{(r)}\right) \right|^{-1/2}}{\sum_{r=1}^{R} \pi\left(\hat{\boldsymbol{\theta}}^{(r)}\right) \left| \mathbf{A}_N\left(\hat{\boldsymbol{\theta}}^{(r)}\right) \right|^{-1/2}} \mathbf{N}\left(\hat{\boldsymbol{\theta}}^{(r)}, \mathbf{A}_N^{-1}\left(\hat{\boldsymbol{\theta}}^{(r)}\right)\right) \tag{23}$$

where $\mathbf{N}(\boldsymbol{\mu}, \boldsymbol{\Sigma})$ denotes a multivariate Gaussian distribution with mean $\boldsymbol{\mu}$ and covariance matrix $\boldsymbol{\Sigma}$. It is assumed that the posterior PDF of the parameters is concentrated in the close neighbourhood of a finite number of optimal points. $\mathbf{A}_N^{-1}$ is the inverse of the Hessian matrix of the function $g(\boldsymbol{\theta}) = \ln J(\boldsymbol{\theta})(N_t N_o - 1)/2$ evaluated at r-th optimal point $\hat{\boldsymbol{\theta}}^{(r)}$ for $r = 1, ..., R$.

Signal envelope and hybrid optimization strategy

In the proposed Bayesian approach, the posterior PDF $p(\boldsymbol{\theta}|D,M_P)$ in equation (20) is maximized to identify the most 'plausible' damage scenario. This can be achieved by minimizing the measure-of-fit function $J(\boldsymbol{\theta})$ in equation (21) while treating the uncertain parameters as unknowns in the optimization. This is, however, a highly nonlinear optimization problem. The direct use of guided wave signals in the measure-of-fit function $J(\boldsymbol{\theta})$ results a large number of local optimums in the parameter space $S(\boldsymbol{\theta})$[32,34]. The current study used the signal envelopes as the data in order to minimize the number of local optimal points in the optimization. In addition, a hybrid optimization strategy was put in place to minimize the measure-of-fit function $J(\boldsymbol{\theta})$ in equation (21), thereby further improving the robustness and efficiency required for solving the optimization problem.

Hilbert transform for signal envelope extraction

The Hilbert transform can be used as a signal processing tool to extract the signal envelope of the guided wave. The Hilbert transform is defined as[5]

$$H(t)=\frac{1}{\pi}\int_{-\infty}^{\infty}\frac{u(t)}{t-\tau}d\tau \tag{24}$$

where $H(t)$ is the Hilbert transform of guided wave signal $u(t)$. Equation (24) performs a 90° phase shift of the signal $u(t)$. An analytic signal can be constructed by

$$u_A(t)=u(t)+iH(t)=H(t)e^{i\varphi(t)} \tag{25}$$

where the envelope u_{env} and instantaneous phase $\varphi(t)$ are defined as

$$u_{env}=\sqrt{u^2(t)+H^2(t)} \quad \text{and} \quad \varphi(t)=\arctan\left[\frac{H(t)}{u(t)}\right] \tag{26}$$

In the present study the Hilbert transform was used to extract the signal envelope of the guided wave calculated using the spectral finite element method and measured in experiments. The damage identification was then carried out using the signal envelopes, i.e. $\tilde{u}(t) = \tilde{u}_{env}(t)$ and $u(t;\boldsymbol{\theta}) = u_{env}(t;\boldsymbol{\theta})$ in equation (21). As the complexity of the signal envelopes is less than the time domain guided wave signal, it reduces the number of the local optimal points in the optimization. This improves the robustness and efficiency of solving the optimization problem.

Hybrid optimization strategy

A hybrid optimization strategy, combining a PSO algorithm and the simplex search method was adopted to solve the optimization problem in equation (21). The global optimum solution of these unknown parameters represents the most 'plausible' damage scenario. PSO is an evolutionary computation technique originally developed to simulate coordinated social behaviour among animals, such as schools of fish or flocks of birds. The idea was first proposed by Kennedy and Eberhart[47]. PSO is a population-based search method that is generally good at finding the global optimal solution, but computationally expensive when we seek to accurately determine the location of the global optimal point. This current study, therefore, experimented with a hybrid optimisation strategy to improve the computational efficiency when seeking to accurately determine the global optimal point. The PSO algorithm is first used to perform global searches in the parameter space $S(\boldsymbol{\theta})$. Once the local potential space is identified, the simplex search method is then used for a local exploitation, searching to accurately determine the global optimal solution.

PSO is based on the particle swarm concept. At the initial stages of optimization, a number of particles are initialized randomly in the parameter space $S(\boldsymbol{\theta})$. The objective function of each of particle is then evaluated at its current position. An iterative process is

carried for N_I times. At m-th iteration, for $m = 1,...,N_I$, an N_D-dimensional vector $\boldsymbol{\theta}_i^m = \{\theta_{i1}^m \theta_{i2}^m,...,\theta_{iN_D}^m\}^T$ is used to represent the position of the i-th particle of the swarm, for $i = 1,...,N_P$, where N_P is the number of population. The position of each particle is a potential solution of the optimization problem. $\mathbf{V}_i^m = \{v_{i1}^m, v_{i2}^m,...,v_{iN_D}^m\}^T$ and $\tilde{\boldsymbol{\theta}}_i^m = \{\tilde{\theta}_{i1}^m, \tilde{\theta}_{i2}^m,...,\tilde{\theta}_{iN_D}^m\}^T$ are used to represent the velocity and the best position of the particle at the m-th iteration, respectively. PSO consists of two main processes, velocity update and position update. At $(m+1)$-th iteration the i-th particle is accelerated toward its previous best position $\tilde{\boldsymbol{\theta}}_i^m$ and the global best position $\tilde{\boldsymbol{\theta}}_g^m$ based on equation (27). The position at $(m+1)$-th iteration is updated using equation (28).

$$\mathbf{V}_i^{m+1} = w^m \mathbf{V}_i^m + \lambda_1 r_1 \left(\tilde{\boldsymbol{\theta}}_i^m - \boldsymbol{\theta}_i^m \right) + \lambda_2 r_2 \left(\tilde{\boldsymbol{\theta}}_g^m - \boldsymbol{\theta}_i^m \right) \tag{27}$$

$$\boldsymbol{\theta}_i^{m+1} = \boldsymbol{\theta}_i^m + \mathbf{V}_i^{m+1} \tag{28}$$

where r_1 and r_2 are random numbers drawn from a uniform distribution on interval [0, 1]. λ_1 and λ_2 are cognitive and social coefficients, which reflect the degree of confidence in the best solution found by each individual particle and by the swarm as a whole, respectively. In this study $\lambda_1 = 0.5$ and $\lambda_2 = 1.25$, which satisfies the stability condition $0 < (\lambda_1 + \lambda_2) < 4$[48]. w^m is the inertia weight at m-th iteration for controlling the exploration abilities of the swarm. The PSO used in the current study adopts a dynamic variation of inertia weight with a linear decrease in each iteration[49]. The inertia weight at $(m+1)$-th iteration is obtained as

$$w^{m+1} = w_I - m \frac{w_I - w_F}{N_I} \tag{29}$$

where w_I and w_F are the initial weight and final weight, and they equal 0.9 and 0.4, respectively, which satisfy the stability condition $0.5(\lambda_1 + \lambda_2) - 1 < w^{m+1} < 1$[48]. N_I is the maximum number of iterations. An advantage of using equation (29) is that the inertia weight is high during initial global searches and subsequently narrows the searches to feasible areas

by decreasing the inertia weight toward the final weight, improving the efficiency and performance of the PSO. The PSO algorithm is summarized below.

1. Initialize a set of particle positions $\mathbf{\theta}_i^1$ and velocities $\mathbf{V}_i^1$ with random distribution in parameter space $S(\mathbf{\theta}) \subset \mathfrak{R}^{N_D}$.
2. Evaluate the objective function value of each particle.
3. Determine the best position of each particle $\tilde{\mathbf{\theta}}_i^m$ and the best global position of the swarm $\tilde{\mathbf{\theta}}_g^m$ at m-th iteration.
4. Update the particle velocities and positions using equations (27) and (28).
5. Repeat steps (2) – (4) until the maximum number of iteration N_I or sufficiently good fitness are met.

Once the PSO identifies the local potential space from the parameter space $S(\mathbf{\theta})$, the simplex search method can be used to accurately determine the global optimum solution using the optimum solution from the initial trial of the PSO. The hybrid optimization strategy tactically consolidates the advantages of PSO and the simplex search method in a search for the global optimum region and the accurate location of the optimum point, respectively, providing an enhanced strategy for solving damage identification problems.

Measurement position effect on guided wave signals

A 3D explicit finite element simulation using LS-DYNA was carried out to provide a preliminary study before the experimental verification. The aim of the preliminary study is to gain a fundamental understanding of the guided wave mode conversion at the damage and provide a validation that the mode conversion from longitudinal wave to flexural wave can be excluded in the measured signals by choosing an appropriate measurement position.

A 2 m long aluminum beam (Grade 6060-T5) with 12×6 mm^2 rectangular cross-section, which is identical to the beam specimens used in the experimental verification, was modeled using the LS-DYNA. Eight-noded 3D reduced integration solid brick elements with hourglass control were used to model the beam, in which each node has threes of freedom. The size of the solid brick elements is 0.4×0.4×0.4 mm^3 that guarantees there are sufficient number of elements exist per wavelength of the longitudinal wave and in the through-thickness direction of the beam. The longitudinal wave was excited by applying the nodal displacement in the longitudinal direction of the surface nodes located at one of the beams end. The excitation signal was an 80 kHz narrow band eight-cycle sinusoidal tone burst pulse modulated by a Hanning window. A step damage located at L_d = 900 mm with d_L = 40 mm and d_d = 2.5 mm was simulated by removing the finite elements.

Figure 2 shows typical time snapshots of the finite element simulated displacement for the beam. Figures 2a and 2b shows snapshots of the simulated longitudinal wave propagation and interaction with the step damage in the beam, respectively. Figure 2c shows the mode conversion from the longitudinal wave to the flexural wave at the step damage and the flexural wave propagates toward the beam end.

Using the coordinate system defined in Figure 2, the x-, y- and z- displacement modeshapes of the fundamental longitudinal and flexural modes at the shorter side of the beam cross-section are shown in Figures 3a and 3b, respectively. As indicated by the modeshape of the longitudinal mode in Figure 3a, the fundamental longitudinal wave propagating in x-direction not only induces the x-displacement but also z-displacement due to the Poisson effect. Hence, the longitudinal wave can be measured through the z-displacement. As shown in Figure 3b, the modeshape of the fundamental flexural mode is quite different compared to the longitudinal mode as shown in Figure 3a. The z-displacement of the fundamental flexural mode has zero magnitude at the center of the shorter side of the beam cross-section. This indicates that the flexural wave can be excluded in the measurements if

the z-displacement is measured at this position. Hence, the Mindlin-Herrmann theory described in the section "Modelling of longitudinal wave in beams with damages" can well predicts the experimental data without considering the mode conversion at the step damage.

As one-dimensional laser Doppler vibrometer was used to measure the longitudinal wave in this study, the displacements were only measured in one direction. Figures 4b – 4d show the simulated signals at $x = 450$ mm away from the excitation location but these signals were measured in different directions and at different y- and z-coordinate locations as shown in Figure 4a. Figure 4b shows the y-displacement at $x = 450$ mm, $y = 6$ mm and $z = 6$ mm, where is the center of the top longer side of the beam cross-section. Both longitudinal and flexural wave exist in the signal measured at this position. Figures 4c and 4d show the x-displacement at $x = 450$ mm, $y = 6$ mm and $z = 0$ mm, and $x = 450$ mm, $y = 3$ mm and $z = 0$ mm, where are top and centre of the shorter side of the beam cross-section, respectively. Comparing the signals in Figure 4c and 4d, it shows that the flexural wave can be excluded in the measured signal for the measurement position at the center of the shorter side of the beam cross-section ($x = 450$ mm, $y = 3$ mm and $z = 0$ mm). The next section will discuss the details of the experimental setup and the signal measured using the laser Doppler vibrometer at this measurement position.

Experimental verification

Experimental setup

Four aluminium beams (Grade 6060-T5), 2 m in length with a 12×6 mm^2 rectangular cross-section, were used as specimens to verify the proposed methodology. A schematic diagram of the experimental setup is shown in Figure 5. A rectangular piezoceramic transducer with dimensions of $12 \times 6 \times 2$ mm^3 was adhesively bonded to the surface of the left end of each of the beam specimens. A $12 \times 6 \times 4$ mm^3 brass mass was attached to the

piezoceramic transducer as a backing mass to increase the excitability of the longitudinal wave, and improve the signal-to-noise ratio. The excitation signal was an 80 kHz narrow-band eight-cycle sinusoidal tone burst pulse modulated by a Hanning window. The reason of selecting this excitation frequency is that better signal-to-noise ratio can be obtained in the measurements. A computer controlled arbitrary wave form generator [Stanford Research DS345] with 10 V peak-to-peak output voltages was used to generate the excitation signal, which was amplified by a factor of 10-50 using a power amplifier [Krohn Hite model 7500]. Pushed through the piezoceramic transducer, the signal produces a longitudinal wave at the left beam end, which is measured by a laser Doppler vibrometer [Polytech OFV 303/OFV 3001].

Based on the understanding of the displacement modeshapes of the fundamental longitudinal and flexural wave mode in the section "Measurement position effect on guided wave signals", the laser measurement position was located at the center of a shorter side of the beam cross-section as shown in Figure 5 to measure the longitudinal wave. At this position, the longitudinal wave can be measured through the out-of-plane motion due to the Poisson effect and the flexural wave can be excluded in the measured signals. The measurement location was 450 mm from the excitation point. The head of the laser Doppler vibrometer was positioned by a computer controlled positioning system [Newport ESP 300] to enhance the accuracy of the measurement location on the beams. The measured signals were then fed into a computer via an oscilloscope. The quality of the measurements was improved by averaging the signals over a number of acquisitions.

Experimental case studies

Four step damages, designated as Cases C1, C2, C3 and C4, were manufactured on four different aluminium beams. The location and length of the step damages were first marked on the beams and then manufactured using milling machine, and hence, there were ±1 mm

measurement uncertainty in the damage location and length, and ±0.5 mm machining tolerance in the damage depth. The performance of the proposed Bayesian approach in identifying the damages was evaluated using a number of experimental case studies. All cases involved step damage at different locations (L_d), lengths (d_L) and depths (d_d) in the beams. Case C1 involved step damage at the greatest damage depth d_d = 2.50 mm. The damage was located at L_d = 1174.75 mm with a damage length of d_L = 50.50 mm. A smaller damage depth of d_d = 2.00 mm was located at L_d = 1062.50 mm (Case C2), but it exhibited a greater damage length of d_L = 75.00 mm. Cases C3 and C4 were assigned the same damage location L_d = 980.00 mm and length d_L = 40.00 mm. The only difference was the damage depths, which were d_d = 2.00 mm and d_d = 1.00 mm in Cases C3 and C4, respectively. Overall, Case C4 was the most challenging situation because of the small damage depth resulting small reflected wave amplitude. A summary of all the damage cases is given in Table 1. The proposed Bayesian approach was employed to identify the damages using the extracted signal envelopes in all cases.

To demonstrate the sensitivity of the longitudinal guided wave to the step damages, the measured time domain guided wave signals and the signal envelopes of Cases C3 and C4 are shown in Figures 6a and 6b. The first pulse is the incident wave and the second pulse is the wave reflected from the damage. The third pulse is the reflected wave from the damage rebounded from the left beam end. As shown in Figure 6a, there was an additional wave pulse immediately after the incident wave. Based on its arrival time, this pulse was found to be a flexural wave caused by the fact that the plane of the piezoceramic transducer was not attached perfectly parallel to the beam end surface. The existence and amplitude of the pulse therefore depended on the care with which the piezoceramic transducers were installed. As described in the experimental setup, a backing mass was attached to the piezoceramic transducer to minimize the additional pulse. Overall, the amplitude of the pulse was

indistinguishable from the reflected waves from the damage, and hence, the impact on damage identification was negligible.

As shown in Figures 6a and 6b, the reflected waves from the damages contained the information of the damage location, length and depth. In theory, damage location was indicated by wave arrival time while the length and depth of the damage could be assessed using wave shape. In practice, however, the identification of the damages from direct observation of the signal was not straightforward, especially for characterization of the damage length, because of the pulse distortion, attenuation, existence of additional wave modes and reflections from boundaries. A Bayesian approach was therefore applied to provide a quantitative identification of the damages in the beams.

Damage identification results and discussions

The proposed Bayesian approach was first applied in Case C1. A summary of the damage identification results is shown in Table 2. The identified damage location, length and depth of Case C1 are $\hat{L}_d = 1140.61$ mm, $\hat{d}_L = 52.28$ mm and $\hat{d}_d = 2.57$ mm. The identified values are very close to the true values (1174.75±1 mm, 50.50±1 mm and 2.50±0.5 mm). The corresponding errors are 2.91%, 3.52% and 2.73% in the damage location, length and depth, respectively. Case C2 considered a damage located at $L_d = 1062.50±1$ mm with greater length ($d_L = 75.00±1$ mm) but with less depth ($d_d = 2.00±0.5$ mm). The identified values are $\hat{L}_d = 1062.50$ mm, $\hat{d}_L = 76.67$ mm and $\hat{d}_d = 2.01$ mm, which are in good agreement with the true values. As an example of how well the predicted signal envelopes match the measured results, a comparison between the signal envelopes predicted by the spectral finite element using the identified values and the measured data for Cases C1 and C2 are shown in Figures 7a and 7b, respectively. The predicted data matches the measured data very well. The figures

also illustrate that it is difficult to identify the damage length from the direct observation of the signals.

Because the proposed damage identification method was developed based on the Bayesian approach, the posterior PDF of the identified damage locations, lengths and depths were also obtained to determine the uncertainties associated with the damage identification results. Figures 8a and 8b show the normalized marginal PDF of the identified damage length and depth for Cases C1 and C2, respectively. The high confidence level of the identified damage characteristics in these two cases is indicated by the PDF value dropping very sharply even for small deviations from the identified damage length and depth. As shown in the Figures 8a and 8b, both cases have similar high confidence level in the identified damage depth. However, the PDF of the identified damage length in Case C2 drop more slowly compared to Case C1. This shows that the uncertainties associated with the identified damage length are higher in Case C2.

The coefficient of variation (COV) of the identified damage parameters were calculated based on the posterior PDFs and summarized in Table 2. The COV is a normalized measure of the dispersion of a probability distribution about its mean value. It provides a convenient way to analyze and compare the uncertainties associated with the identified damage parameters. As shown in Table 2, the COV of the identified damage locations (0.01% in Case C1 and 0.03% in Case C2) was relatively small compared to the COV of the identified damage lengths (0.08% in Case C1 and 0.19% in Case C2) and depths (0.29% in Case C1 and 0.33% in Case C2), which means that the identified damage locations have less uncertainties associated with the identified damage lengths and depths. This is consistent with the fact that guided waves can provide accurate information related to damage location[13].

The damage identification results of Cases C3 and C4 are also summarized in Table 2. The damages in these two cases were at the same location and had the same damage length. The only difference is the lower damage depth in Case C3 (d_d=2.00±0.5 mm) compared with

Case C4 (d_d=1.00±0.5 mm). Using the proposed Bayesian approach, the identified values were $\hat{L}_d$ = 952.340 mm, $\hat{d}_L$ = 46.42 mm and $\hat{d}_d$ = 1.91 mm and $\hat{L}_d$ = 953.91 mm, $\hat{d}_L$ = 37.82 mm and $\hat{d}_d$ = 1.13 mm for Cases C3 and C4, respectively. All the identification values exhibited a reasonable agreement with the true values. The results show that the proposed damage identification method has no problem identifying the damage, even when the damage depth is very small.

The COV of the identified value in Cases C3 (0.46% for damage length and 0.45% for damage depth) and C4 (0.78% for damage length and 1.96% for damage depth) shows that lower damage depth leads to large uncertainty in damage identification because shallow damage produces a reduced amplitude wave, i.e. smaller signal-to-noise ratio. There is less damage information offered by the measured data, increasing the uncertainties associated with the identified values.

Conclusions

This paper presented a Bayesian approach for damage identification in beams using longitudinal guided wave signals. Signal envelopes extracted using the Hilbert transform and a hybrid PSO algorithm were proposed to enhance damage identification. The proposed method was verified through a number of experimental case studies. Aluminium beams with different damage scenarios were used to investigate the ability of the proposed Bayesian method to identify structural damage location, length and depth. Very encouraging results were obtained from the experimental case studies. The results show that the proposed method is able to accurately identify the damages even in cases the damage depths were relatively small. The method is also cost effective in terms of instrumentation as the damages can be identified in long structures based on the guided waves measured at a single location. In addition the uncertainties associated with the damage identification results can be quantified,

although the uncertainties of the identified damage parameters increase with smaller damage depths as less damage information is contained in the waves reflected from the damages. It is worth noting that although the current study focused on laminar type of damage, the proposed method is general and applicable to different types of damages or more complex engineering structures by modifying the embedded spectral finite element model in the Bayesian statistical framework. In practical situations, the types of damages could usually be pre-determined based on engineering judgment and the material composition of the damaged structures, and hence, the proposed Bayesian damage identification approach is feasible for practical applications.

Acknowledgement

References

1. Achenbach JD. Quantitative nondestructive evaluation. *Inter J Solids Struct* 2000; 37: 13-27.

2. Rose JL. A baseline and vision of ultrasonic guided wave inspection potential. *J Pressure Vessel Tech* 2002; 124: 273-282.

3. Chang PC, Flatau A and Liu SC. Review paper: health monitoring of civil infrastructure. *Struct Health Monitor* 2003; 2: 257-267.

4. Sohn H, Farrar CR, Hernez FM, et al. A review of structural health monitoring literature: 1996-2001. Report no. LA-13976-MS. Los Alamos, N.M.: Los Alamos National Laboratory 2004.

5. Staszewski WJ, Boller C, Tomlinson G. Health monitoring of aerospace structures: smart sensor technologies and signal processing, West Sussex, Wiley, 2004.

6. Farrar CR and Worden K. An introduction to structural health monitoring. *Phil Trans R Soc A* 2007; 365: 303-315.

7. Giurgiutiu V and Soutis C. Enhanced composites integrity through structural health monitoring. *App Compos Mater* 2012; 5: 813-829.

8. Carden EP and Fanning P. Vibration based condition monitoring: a review. *Struct Health Monitor* 2004; 3: 355-377.

9. Khoo LM, Mantena PR and Jadhav P. Structural damage assessment using vibration modal analysis. *Struct Health Monitor* 2004; 3: 177-194.

10. Hamey CS, Lestari W, Qiao P et al. Experimental damage identification of carbon/epoxy composite beams using curvature mode shapes. *Sturct Health Monitor* 2004; 3: 333-353.

11. Lam HF, Ng CT and Leung AYT. Multicrack detection on semirigidly connected beams utilizing dynamic data. *J Eng Mech ASCE* 2008; 134: 90-99.

12. Xu B, Song, G and Masri SF. Damage detection for a frame structure model using vibration displacement measurement. *Struct Health Monitor 2012*; 11: 281-292.

13. Giurgiutiu VB and Zhao W. Piezoelectric wafer active sensor embedded ultrasonics in beams and plates. *Soc Exp Mech* 2003; 43: 428-449.

14. Veidt M and Ng CT. Influence of stacking sequence on scattering characteristics of the fundamental anti-symmetric Lamb wave at through holes in composite laminates. *J Acoust Soc Am* 2011; 129: 1280-1287.

15. Ng CT and Veidt M. Scattering of the fundamental anti-symmetric Lamb wave at delaminations in composite laminates. *J Acoust Soc Am* 2011; 129: 1288-1296.

16. Cho H and Lissenden C. Structural health monitoring of fatigue crack growth in plate structures with ultrasonic guided waves. *Struct Health Monitor* 2012; 11: 393-404.

17. Ng CT and Veidt M. Scattering analysis of Lamb waves from debondings at structural features in composite laminates. *J Acoust Soc Am* 2012; 132: 115-123.

18. Ng CT, Veidt M, Rose LRF. Analytical and finite element prediction of lamb wave scattering at delaminations in quasi-isotropic composite laminate. *J Sound Vib* 2012; 331: 4870-4883.

19. Donskoy D, Sutin A and Ekimov A. Nonlinear acoustic interaction on contact interfaces and its use for nondestructive testing. *NDT&E Inter* 2001; 34: 231-223.

20. Yoder NC and Adams DE. Vibro-acoustic modulation utilizing a swept probing signal for robust crack detection. *Struct Health Monitor* 2010; 9: 257-267.

21. Klepka A, Staszewski WJ, Jenal RB, Szwedo M, Iwaniec J and Uhi T. Nonlinear acoustics for fatigue crack detection – experimental investigations of vibro-acoustic wave modulations. *Struct health Monitor* 2011; 11: 197-211.

22. Rucka, M. Experimental and numerical studies of guided wave damage detection in bars with structural discontinuities. *Arch Appl Mech* 2010; 80: 1371-1390.

23. Lowe MJS, Alleyne DN and Cawley P. Defect detection in pipes using guided waves. *Ultrasonics* 1998; 36: 147-154.

24. Demma A, Cawley P and Lowe M. The reflection of the fundamental torsional mode from cracks and notches in pipes. *J Acoust Soc Am* 2003; 114: 611-625.

25. Lovstad A and Cawley P. The reflection of the fundamental torsional mode from pit clusters in pipes. *NDT & E Inter* 2012; 46: 83-93.

26. Quek ST, Tua PS and Wang Q. Detecting anomalies in beams and plate based on the Hilbert-Huang transform of real signals. *Smart Mater Struct* 2003; 12: 447-460.

27. Li Z, Xia S, Wang J *et al*. Damage detection of cracked beams based on wavelet transform. *Inter J Impact Eng* 2006; 32: 1190-1200.

28. Grabowska J. Palacz M. and Krawczuk M. Damage identification by wavelet analysis. *Mech Syst Signal Process* 2008; 22: 1623-1635.

29. Sun K, Meng G, Li F *et al*. Damage identification in thick steel beam based on guided ultrasonic waves. *J Intell Mater Syst Struct* 2010; 21: 225-232.

30. Zhu X, Rizzo P, Marzani A *et al*. Ultrasonic guided waves for nondestructive evaluation/structural health monitoring of trusses. *Meas Sci Technol* 2010; 21(045701): 1-12.

31. Liew CK and Veidt M. Pattern recognition of guided waves for damage evaluation in bars. *Pattern Recog Letters* 2009; 30: 321-330.

32. Nag A, Roy Mahapatra D, Gopalakrishnan S. Identification of delamination in composite beams using spectral estimation and a genetic algorithm. *Smart Mater Struct* 2002; 11: 899-908.

33. Krawczuk M. Application of spectral beam finite element with a crack and iterative search technique for damage detection. *Finite Elem Analy Design* 2002; 38: 537-548.

34. Ng CT, Veidt M and Lam HF. Guided wave damage characterisation in beams utilising probabilistic optimisation. *Eng Struct* 2009; 31: 2842-2850.

35. Pau A. and Vestroni F. Wave propagation in one-dimensional waveguides for damage characterization. *J Intell Mater Syst Struct* 2011; 22: 1869-1877.

36. Beck JL and Katafygiotis LS. Updating models and their uncertainties I: Bayesian statistical framework. *J Eng Mech ASCE* 1998; 124: 455-461.

37. Doyle JF. Wave propagation in structures spectral analysis using fast discrete Fourier transforms, 2nd ed, Springer, 1997.

38. Park I, Kim S and Lee U. Dynamics and guided waves in a smart Timoshenko beam with lateral contraction. *Smart Mater Struct* 2013; 22(075034): 1-15.

39. Krawczuk M, Grabowska J and Palacz M. Longitudinal wave propagation Part I − Comparison of rod theories. *J Sound Vib* 2006; 295: 461-478.

40. Jean-Pierre D and Tisseur F. Perturbation theory for homogeneous polynomial eigenvalue problem. *Linear Algebra Appl* 2003; 358: 71-94.

41. Papadimitriou C, Beck JL and Au SK. Entropy-based optimal sensor location for structural model updating. *J Vib Control* 2000; 6: 781-800.

42. Flynn EB and Todd MD. A Bayesian approach to optimal sensor placement for structural health monitoring with application to active sensing. *Mech Sys Sig Proc* 2010; 24: 891-903.

43. Vanik MW, Beck JL and Au SK. Bayesian probabilistic approach to structural health monitoring. *J Eng Mech ASCE* 2000; 126: 738-745.

44. Flynn EB, Todd MD, Wilcox PD, Drinkwater BW and Croxford AJ. Maximum-likelihood estimation of damage location in guided-wave structural health monitoring. *Proc Royal Soc A* 2011; 467: 2575-2596.

45. Flynn EB, Todd MD, Croxford AJ, Drinkwater BW and Wilcox PD. Enhanced detection through low-order stochastic modelling for guided-wave structural health monitoring. *Struct Health Montior* 2012; 11: 149-160.

46. Papadimitriou C, Beck JL and Katafygiotis LS. Asymptotic expansions for reliability and moments of uncertain systems. *J Eng Mech ASCE* 1997; 123: 1219-1229.

47. Kennedy J and Eberhart RC. Particle swarm optimization. In: *Proceedings of IEEE International Conference on Neural Networks IV*, Perth, Australia, 27 November – 1 December 1995, pp. 1942-1948.

48. Perez RE and Behdinan K. Particle swarm approach for structural design optimization. *Comp Struct* 2007; 85:1579-1588.

49. Shi Y and Eberhar R. A modified particle swarm optimizer. In: *Proceeding of IEEE International Conference on Evolutionary Computation*, IEEE Press, Piscataway, NJ, USA, 1998, pp. 69-73.
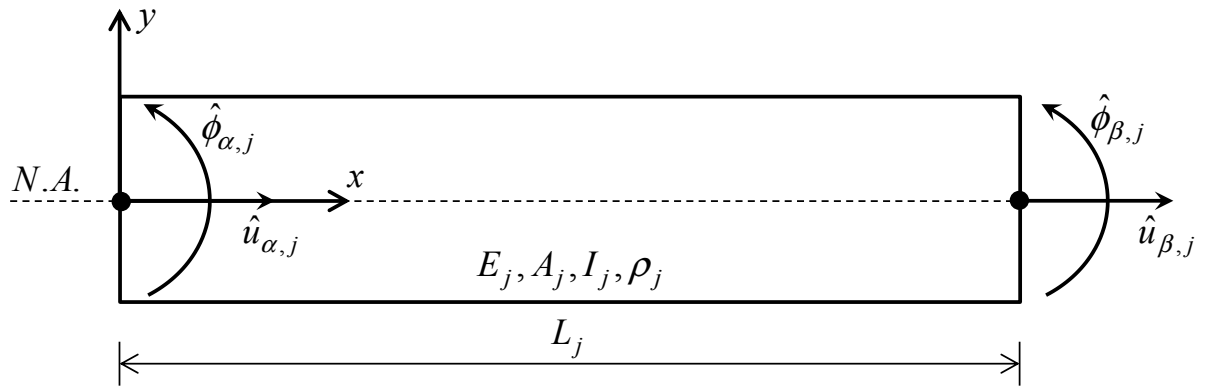
Figures List

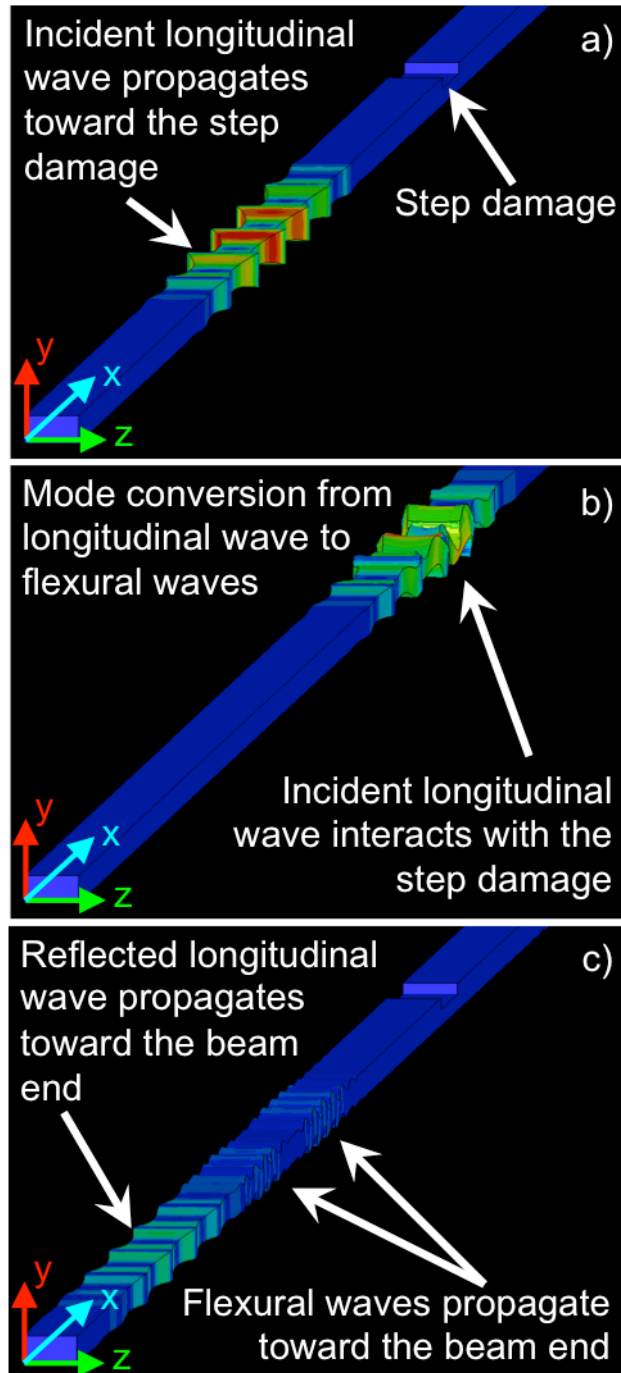Figure 1. Spectral finite element based on the Mindlin-Herrmann theory

Figure 2. Typical contour snapshots of finite element simulated displacement for the beam: (a) incident longitudinal wave, (b) incident longitudinal wave interacts with the step damage, and (c) mode conversion from longitudinal wave to flexural wave at the step damage.
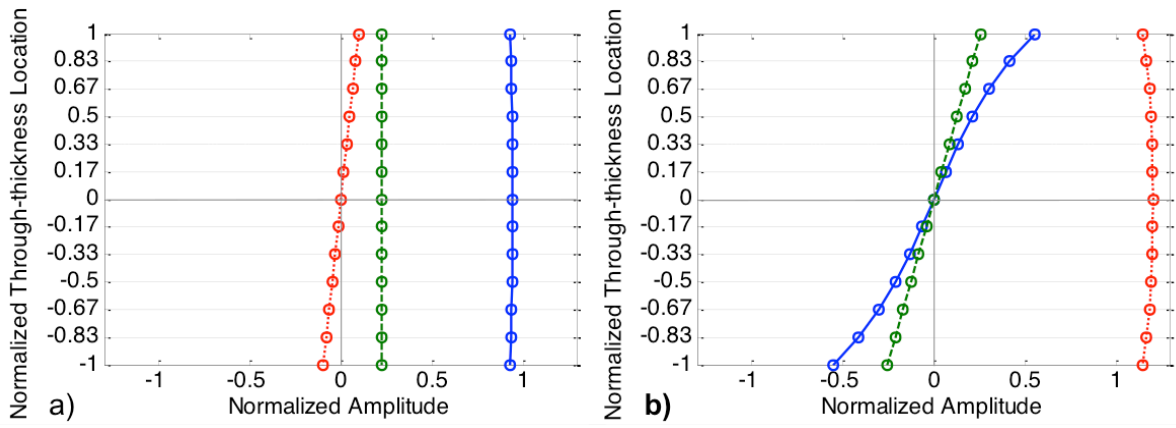
Figure 3. Fundamental (a) longitudinal and (b) flexural mode displacement modeshapes at the shorter side of the beam cross-section at 80 kHz (solid line with circles: x-displacement; dotted line with circles: y-displacement; dashed line with circles: z-displacement).
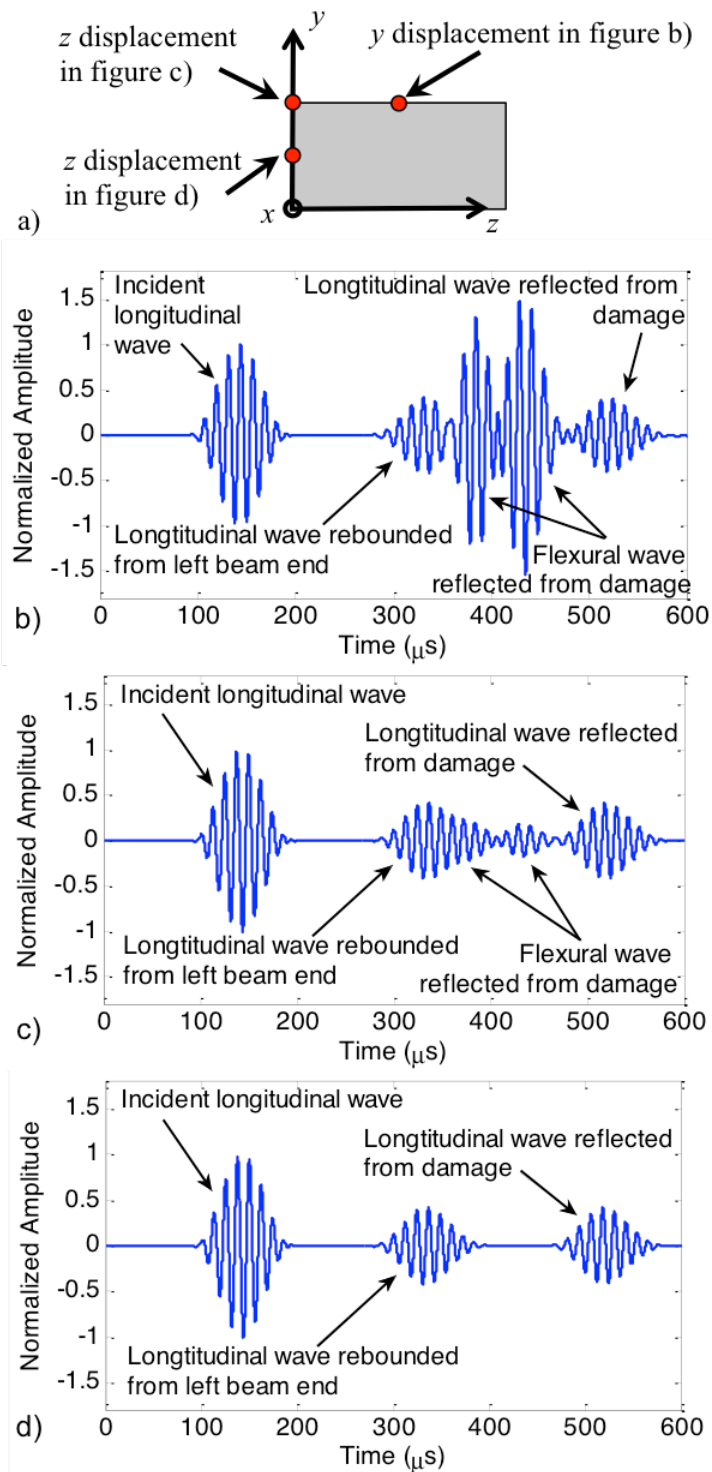
Figure 4. (a) Measurement positions of the beam cross-section located at x = 450 mm. Finite element simulated (b) y- displacement signal at y = 6 mm, z = 6 mm and z-displacement signal at (c) y = 6 mm and z = 0 mm; and (d) y = 3 mm and z = 0 mm.
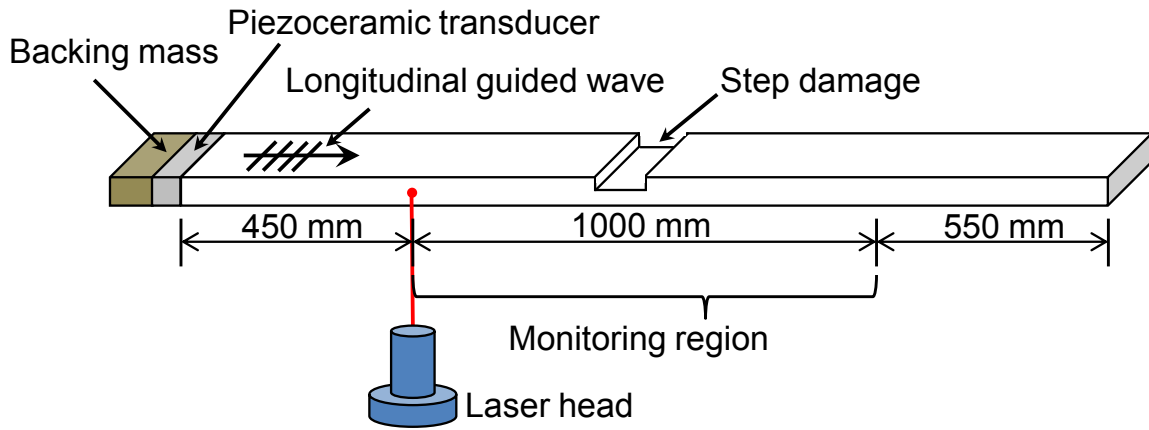
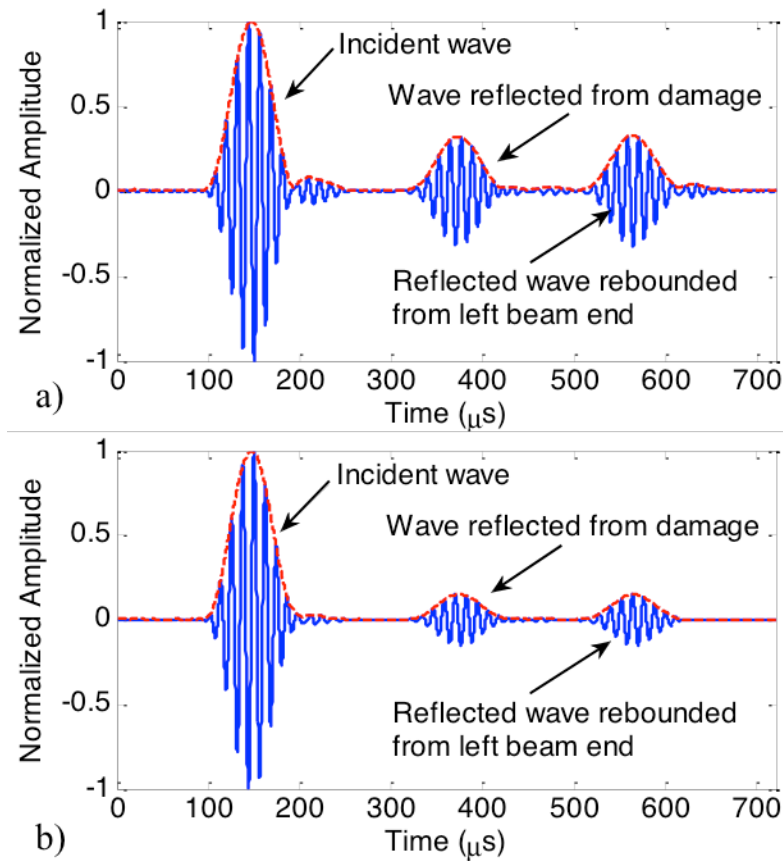Figure 5. Schematic diagram of the experimental setup.

Figure 6. Experimental measured time domain signal (solid line) and signal envelope (dashed line) for Cases (a) C3 and (b) C4.
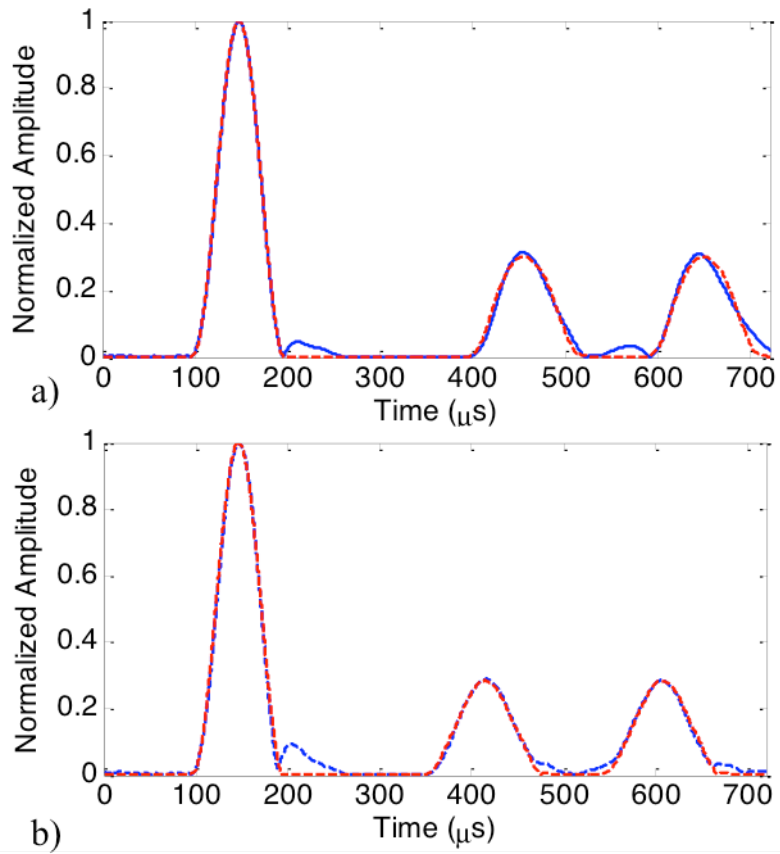
Figure 7. Comparison of the predicted and measured guided wave signal for Cases (a) C1 and (b) C2 (solid line: prediction using identified parameters; dashed line: experimental data).
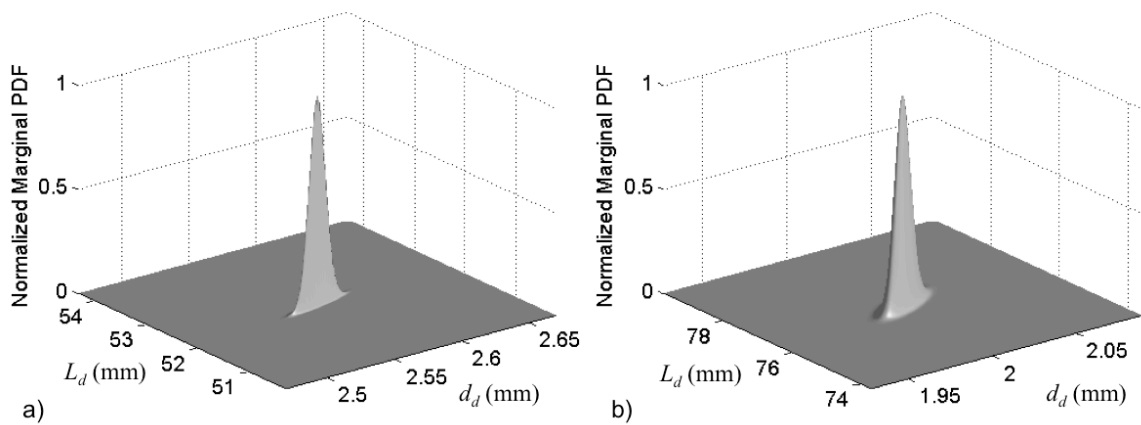

Figure 8. Normalized marginal PDF of the damage length and depth for Cases (a) C1 and (b) C2.

Tables List

Table 1. Summary of all damage cases in the experimental case studies

Case	Damage location (L_d) (mm)	Damage length (d_L) (mm)	Damage depth (d_d) (mm)
C1	1174.75±1	50.50±1	2.50±0.5
C2	1062.50±1	75.00±1	2.00±0.5
C3	980.00±1	40.00±1	2.00±0.5
C4	980.00±1	40.00±1	1.00±0.5

Table 2. Summary of the results in damage identification

Case	Damage location (mm)		Damage length (mm)		Damage depth (mm)	
	Identified value ($\hat{L}_d$)	True value (L_d)	Identified value ($\hat{d}_L$)	True value (d_L)	Identified value ($\hat{d}_d$)	True value (d_d)
C1	1140.61 (0.01%)	1174.75±1	52.28 (0.08%)	50.50±1	2.57 (0.29%)	2.50±0.5
C2	1040.10 (0.03%)	1062.50±1	76.67 (0.19%)	75.00±1	2.01 (0.33%)	2.00±0.5
C3	952.34 (0.03%)	980.00±1	46.42 (0.46%)	40.00±1	1.91 (0.45%)	2.00±0.5
C4	953.91 (0.03%)	980.00±1	37.82 (0.78%)	40.00±1	1.13 (1.96%)	1.00±0.5

Note: Values in brackets are the coefficient of variation (COV)